Sensing Ultrasound Localization Microscopy for the visualization of glomeruli in living rats and humans

Louise Denis, Sylvain Bodard, Vincent Hingot, Arthur Chavignon, Jacques Battaglia, Gilles Renault, Franck Lager, Abderrahmane Aissani, Olivier Hélénon, Jean-Michel Correas, et al.

Sensing Ultrasound Localization Microscopy for the visualization of glomeruli in living rats and humans

Louise Denis[1#*], Sylvain Bodard[1,2,3#], Vincent Hingot[1], Arthur Chavignon[1], Jacques Battaglia[1], Gilles Renault[4], Franck Lager[4], Abderrahmane Aissani[1], Olivier Hélénon[2,3], Jean-Michel Correas[1,2,3], Olivier Couture[1]

# These authors contributed equally to this work

* Corresponding author: louise.denis@sorbonne-universite.fr

[1] Sorbonne Université, CNRS, INSERM Laboratoire d'Imagerie Biomédicale, F-75006, Paris, France

[2] AP-HP, Hôpital Necker Enfants Malades, Service d'Imagerie Adulte, F-75015, Paris, France

[3] Université de Paris Cité, F-75006, Paris, France

[4] Université de Paris, Institut Cochin, INSERM, CNRS, F-75014 PARIS, France

Summary

Background

Estimation of glomerular function is necessary to diagnose kidney diseases. However, the study of glomeruli in the clinic is currently done indirectly through urine and blood tests. A recent imaging technique called Ultrasound Localization Microscopy (ULM) has appeared. It is based on the ability to record continuous movements of individual microbubbles in the bloodstream. Although ULM improved the resolution of vascular imaging up to tenfold, the imaging of the smallest vessels had yet to be reported.

Methods

We acquired ultrasound sequences from living humans and rats and then applied filters to divide the data set into slow-moving and fast-moving microbubbles. We performed a double tracking to highlight and characterize populations of microbubbles with singular behaviors. We decided to call this technique “sensing ULM” (sULM). We used post-mortem micro-CT for side-by-side confirmation in rats.

Findings

In this study, we report the observation of microbubbles flowing in the glomeruli in living humans and rats. We present a set of analysis tools to extract quantitative information from individual microbubbles, such as remanence time or normalized distance.

Interpretation

As glomeruli play a key role in kidney function, it would be possible that their observation yields a deeper understanding of the kidney. It could also be a tool to diagnose kidney diseases in patients. More generally, it will bring imaging capabilities closer to the functional units of organs, which is a key to understand most diseases, such as cancer, diabetes, or kidney failures.

Funding

This study was funded by the European Research Council under the European Union Horizon H2020 program (ERC Consolidator grant agreement No 772786-ResolveStroke).

Keywords

sensing Ultrasound Localization Microscopy, super resolution, glomeruli, human kidney, rat kidney, in vivo

Research in Context

Evidence before this study

Kidneys are highly vascularized organs and the observation of vessels permits the diagnosis and the prognosis of kidney diseases. In clinical practice, the assessment of renal microcirculation is done indirectly by urinary or blood tests. Although techniques have emerged to directly observe the renal vasculature at the microscopic level (micro-CT, histology), they remain ex-vivo or invasive imaging.

Ultrasound Localization Microscopy (ULM) has been introduced and has proven its ability to map the renal vasculature at a microscopic scale in vivo on mice, rats, and humans. Due to the low sensitivity of ULM on very slow microbubbles, the small vessels present in the renal glomeruli have not yet been observed.

The added value of this study

In this study, we filtered the ultrasound acquisitions twice and thus made ULM sensitive to various microbubble dynamics, including those flowing in glomeruli. By tracking fast and slow microbubbles separately, we were able to image in vivo glomeruli noninvasively on rats and human grafts. With this technique, we were also able to measure quantitative information - such as the relative number of glomeruli - which may be biomarkers of many kidney diseases. Such an approach has been called “sensing Ultrasound Localization Microscopy” (sULM).

Implications of all the available evidence

This study proves the ability of sULM to map glomeruli in 2D with both a research ultrasound scanner for rats and a clinical ultrasound scanner for humans. We believe that this study could be extended worldwide thanks to the availability of the code and the common scanner used in humans. Glomeruli observation and quantification could become a diagnostic tool for many kidney diseases, such as hypertension, diabetes, autoimmune diseases, and cancer. Due to sULM’s ability to track and classify the individual behavior of each microbubble, we strongly believe that this study reduces the gap between macroscopic imaging and metabolism analyses.

Introduction

Medical imaging modalities provide an invaluable window at the organ scale deep in the human body. Meanwhile, within thin slices of biopsies or shallow depths, optical microscopy reveals cellular morphology and mechanism. Both are necessary for clinical diagnosis and fundamental studies, but the information they provide remains incomplete. Indeed, the functional units of many organs reside at an intermediate scale, tens of micrometers in size, within multicellular units too small to be observed with medical imaging and too deep for microscopy to visualize non-invasively.

To observe such a mesoscale, we previously introduced Ultrasound Localization Microscopy (ULM)[1–3], which is an acoustic super-resolution technique that can map the microcirculation with unprecedented resolution at the scale of the organ of a living animal[4–9]. It relies on the tracking[10] of isolated clinical contrast agents, namely microbubbles, traveling within the blood vessels. Since then, it has been investigated in humans[11–13]. Although it provides a rich microvascular mapping, it still remains blind to the functional units of organs. This is because very slow microbubbles within capillary beds are difficult to distinguish[14].

Here, we present a "sensing ULM" method using the microbubble as a sensor of its immediate environment (sULM). Such accuracy allows to classify particular microbubble motion patterns corresponding to expected microscopic structures. Thanks to filtering methods adapted to the movement of the microbubble, we can track the entirety of its dynamics, including its slowest movements. By applying sULM to the kidneys of humans and rats, we aim to observe the organ functional units, i.e. the glomeruli. This component of the nephron is a bundle of capillaries situated between two resistance vessels that provide its filtration force[15]. The glomerulus is impacted by several chronic diseases such as hypertension, diabetes, autoimmune diseases, and cancer that can lead to its destruction and the loss of its filtration functions[16-19]. Imaging of glomeruli is needed for the exploration, diagnosis, and understanding of these pathologies. The problem is that the human glomeruli diameter is approximately 200 microns[20], which is well below the resolution limit of most medical imaging techniques. Clinical imaging techniques cannot provide the observation of individual glomeruli[21–23]. Currently, in the clinic, the glomerulus function is only assessed indirectly either by blood or urine tests that provide access to the global glomerular filtration rate.

In this study, we report the direct observation of individual glomerular structures in the kidney using sULM in humans with a setup available widely in hospitals. We first studied the behavior of microbubbles in glomeruli, on rat kidneys. We then compared sULM to micro-CT considered as a gold standard for glomeruli observation[24–26]. Finally, we demonstrated that the observation of glomeruli by sULM is also possible on human transplanted kidneys. We provide materials, such as post-processing codes, to reproduce these experiments in hospitals equipped with conventional ultrasound scanners.

Methods

Animals ethics

All animal experiments were performed in accordance with the ARRIVE guidelines and approved by the local ethics committee (ethics committee on animal experimentation n°034, Department of Regulated Research Practices Animals Used for Scientific Purposes Unit – AfiS, reference number APAFIS #33913-2021082311153607) between January and May 2022. The number of animals in our study was kept to the necessary minimum. Experiments were performed on 15 Wistar male rats (Janvier Labs, Charles River, Envigo) aged between 8 and 12 weeks. 8 rats were planned to set up the study, in particular on questions of perfusion of the micro-CT. The 7 others were planned to optimize the implementation of the sULM technique. Animals arrived in the laboratory (Institut Cochin, INSERM U1016) 12 hours before the beginning of the experiments. When rats underwent micro-CT examination, they succumbed during contrast injection still under isoflurane anesthesia, i.e. induction at 4 %, maintenance at 2·5% in air. Four rats were used to optimize micro-CT injection. The remaining 11 rats were used to perform sULM. Of these 11, six were scanned by micro-CT. The other five died during the micro-CT injection procedure.

Contrast ultrasound data acquisitions on rats

30 minutes before the start of the ultrasound data acquisition, 330µl/100g of buprenorphine was injected to prevent pain. The rat was then placed in the isoflurane induction cage. Once asleep, we placed it in the supine position on a thermostatically controlled warming tray under isoflurane anesthesia (Fig 1. a). An ophthalmic gel was applied to its eyes to avoid their drying. The temperature of the rat was controlled via a rectal probe and maintained between 35 and 37°C. The animal was shaved and then depilated on the abdomen, opposite the left kidney. The absence of a pinch reflex was verified before the placement of a 25G caudal venous catheter. The left kidney was externalized thanks to a short abdominal wall incision of less than one centimeter. The kidney was then stabilized with two needles on a thin plastic plate and explored by the direct contact of the ultrasound probe, assured by an ultrasound gel.

Ultrasound acquisitions were performed with an ultrasound scanner (Vantage 256, Verasonics, Kirkland) and a linear ultrasound probe L22-14v at a frequency of 15MHz (Verasonics, bandwidth [14-22] MHz, pitch 0·10mm). The probe was positioned longitudinally to the kidney with a real-time B-mode display (Fig 1. b). A microbubbles infusion (Sonovue®, Bracco, Milan, Italy, 8µL of sulfur hexafluoride/mL) of 13 µl/min that lasted two to three minutes was then performed (Supplementary Table 1).

Ultrasound acquisitions were acquired at a frame rate of 500 Hz, a pulse repetition frequency of 12,000Hz, a pixel size of 50µm, and a voltage of 8V. A total of [60-90] blocks were saved, each consisting of 800 images resulting from a compound of 3 angles. The data were then beamformed using a conventional delay-and-sum algorithm.

We removed blocks containing the bolus starts and movements too large to perform the post-processing (see data sharing statement).

Power Doppler performed with the same acquisition and a high threshold SVD is presented in Figure 1c (parameters in Supplementary Table 1).

Micro Computed Tomography (micro-CT) data acquisitions on rats

Once the ultrasound acquisitions were completed, the rat was kept under isoflurane anesthesia to proceed with the injection of the micro-CT contrast agent. This contrast agent is a mixture of barium sulfate (Micropaque 100g, Guerbet, France), PBS (Phosphate Buffer Saline, Cochin INSERM U1016), and gelatin. Gelatin was dissolved at 90°C, then mixed with Micropaque at 40°C to obtain a homogeneous solution, and then stored at a temperature of 4°C[27]. After opening the thorax, a catheter was placed in the left ventricle of the heart, and the right atrium was sectioned to let the liquid flow out, after passing by all the organs. We then injected 25µL of heparin to avoid blood clotting, i.e. vial of 25,000 units by 5,000 units/mL. Then, a 200mL contrast agent heated in a water bath at 42°C was injected at a flow rate of 750mL/h to ensure perfusion of the vasculature. The death of the animal occurred under anesthesia due to this step of injection of the micro-CT contrast medium.
The kidney was kept for 48h in a petri dish in 4% of PFA to fix the perfusion until it was scanned with a high-resolution micro-CT Skyscan 1172 (Bruker, URP2496) with a 5µm voxel size.

Micro-CT and sULM registration

We performed manually the registration between sULM and micro-CT based on the similarity of large vessels (Supplementary Fig. 1). This step was done with the Amira software (ThermoFisher, 2019.4). We averaged 32 micro-CT slices to obtain a 160µm thickness, i.e. the probe elevation resolution. We had a 1,024 by 1,024 matrix of 15µm pixel elements as the output of the Amira registration which we then analyzed in MATLAB.

Perfusion index in micro-CT and noise reduction

To compare micro-CT perfusion in rats, we defined a perfusion metric as the sum of pixels with a value greater than an arbitrary threshold of 0·5 divided by the total number of pixels within the cortex, with the micro-CT matrix normalized by its maximum. In the Supplementary Table 2, we could see that on 3 rats over 6, perfusion was above 5%, which means that the vessels were less contrasted then in the 3 other rats (Supplementary Fig. 2). To reduce these differences in contrast between the vessels, we subtracted noise from micro-CT slices before summing them, i.e. subtraction of the lowest 10% of values within the kidney. This 10% threshold was arbitrarily chosen.

Human ethics

The Ethics Committee of the French Society of Radiology approved this study (CERF, reference number CRM-2203-240). All human acquisitions were performed by following the SRQR guidelines. Informed consent has been obtained from all patients.
Male and female kidney transplanted patients were included from February to August 2020, at Necker Hospital (APHP, France). These subjects were present due to their clinical routine ultrasound examination and no supplementary experimentation was made. Contrast-Enhanced Ultrasound Sequence (CEUS) was performed on patients to search for hypo-vascular areas and necrosis. To obtain the best quality images, the patients were lying in a supine position and breathing slowly during the acquisition. 14 patients were included in this study, and the results of five of them are presented here (three females/two males). The exclusion of the others was mainly due to respiratory motion.

Contrast ultrasound data acquisitions on humans

Data acquisitions on humans were acquired with CEUS embedded in the clinical ultrasound scanner Applio i800 (Canon MS, Nasu, Japan) and a convex abdominal probe i8cX1 (3MHz, Canon, bandwidth [1·8-6·2] MHz), with an injection of a bolus of 1·2mL of contrast agent (Sonovue®, Bracco, Milan, Italy, 8µL of sulfur hexafluoride/mL). CEUS had the advantage to enhance the signal of the microbubbles and allow a better visualization of their behavior. The mechanical index was reduced to 0·07 during the acquisition process to reduce the destruction of the microbubbles and exploit their nonlinear properties. The frame rate was different for each patient due to imaging depth differences, i.e. between 14 and 64Hz. Data acquisition duration, which corresponds to a video clip screenshot of the clinical ultrasound scanner, varied from one to three minutes (Supplementary Table 3). Clips were then divided into blocks of 200 frames each to proceed to sULM. All data were anonymized and stored on an external USB disk to be post-processed in our laboratory.

sULM post-processing

The codes that allowed the reconstruction of vascular mapping by sULM are available in the following GitHub repository: https://github.com/EngineerJB/akebia. A standalone application named Akebia - usable without a MATLAB license - is available in the same repository.

Several classical sULM steps have been applied to each block to obtain a density map. These are very similar in humans and rats so both will be described in this same section.

The first step consisted of a bandpass temporal (for humans) or spatiotemporal singular value decomposition filter (for rats). Frequency cutoff varied from 0·5 to 8·5Hz in the first case and was fixed at 40/800 eigenvalues for the second one. Data were filtered a second time in rats with a low-threshold SVD cumulated to a bandpass filter respectively to highlight slower microbubbles and to remove surrounding tissue (Supplementary Table 1). This way, our datasets were split into two parts: high-speed microbubbles flow with the first filter and slower microbubbles with CEUS for humans and with low-threshold SVD for rats. Previous studies showed that ULM performed better with a split dataset[12].

The second step consisted in the localization of the center of the microbubbles. In humans, this was done with a 2D Gaussian filter and targeting of the regional maximums. In rats, we applied the radial symmetry method to localize the microbubbles' center[28]. Thus, we obtained the positions of the microbubbles in lateral and axial dimensions in pixels unit initially fixed by the acquisition itself, i.e. a pixel size between 70 and 150µm in humans, and 50µm in rats. At this step, we also had the temporal information which is the number of the frame where the microbubble appeared.

The third step consisted in applying the Hungarian algorithm method[29] with the simple tracker Toolbox[10]. We paired frame-to-frame microbubbles with specific constraints to track them. In our case, low-speed and fast-speed tracking parameters were summarized in Supplementary Tables 1 and 3.

We repeated all the precedent steps in each block of our two datasets. Thus, we accumulated all microbubble tracks of all acquisitions twice. In this way, we reconstructed the sULM composite density map. Slow flow speed track accumulation on one side and fast flow speed track accumulation on the other side.

With an interpolation step performed just before track accumulation, the final rats' sULM density maps had a pixel size of 20µm. For humans, clips were already interpolated in the clinical ultrasound scanner, so we kept the same pixel size as the original acquisitions.

All data were processed and analyzed with MATLAB.

Manual segmentation and track classification

Kidney regions were manually delimited on sULM maps in three parts, i.e. cortex, medulla, and major vessels - including renal, interlobar, arcuate vessels, and finer structures such as afferent and efferent arterioles.
To study the behavior of microbubbles in each region, the tracks were then labeled. If one of their points belonged to the masks, then they were marked as belonging to that area.
The segmentation of these three regions was performed similarly in rats and humans.

Glomerular mask creation

A glomeruli-specific mask was then created by considering the normalized distance value of the cortex tracks (see metrics calculation section). These normalized distance values were projected onto the same reconstruction grid used to create the sULM density maps. We then arbitrarily selected pixels whose normalized distance was greater than the 90th percentile of all pixel values by smoothing the image with a Gaussian filter. By drawing a circle of the order of the glomerulus radius from these pixels - i.e. 100µm in humans[20], and 50µm in rats[30] - we thus determined a glomerular mask. We applied the same procedure of track conservation as before. If at least one of its points belonged to the glomerular mask, we labeled the track as belonging to glomeruli.

Metrics calculation

The normalized distance metric was defined as the cumulative distance of a track, divided by the distance separating its first point p_1 to its last one p_n[31].

$$Normalized\ distance = \frac{\sum_{x=1}^{n-1} ||p_x - p_{x+1}||}{||p_1 - p_n||}$$

The remanence time metric has been established as the period (in seconds) during which a microbubble was tracked inside a circle of glomerular size, - i.e. radius of 100µm in humans[20], and 50µm in rats[30]. The center is defined as the median point of the list of points constituting the track.
The dispersity corresponded to the number of times that a track went in the same direction with a tolerance of more or less 20° - taking rounded localization of each track - divided by the number of points constituting the track (Supplementary Fig. 3).

Glomeruli count and perfused distribution width (PDW) calculation

The glomeruli count on the micro-CT was performed with the imregionalmax function of MATLAB in the cortex region on which we applied a Gaussian filter. We arbitrarily chose to keep the pixels with an intensity higher than the 90th percentile of the whole area. The glomeruli count on the sULM has been detailed in the section "Glomerular Mask Creation". We proceeded with manual segmentation of the renal capsule to perform a count of glomeruli based on their distance from it (Supplementary Fig. 1).
We chose to represent the spatial distribution of glomeruli by the histogram of 20 bins for sULM. We used "auto" as a bin method in Matlab. This method worked in several steps. First, the Scotts rule was used to determine the width of the bins. Then bin picker function adjusted the bin width depending on its order of

magnitude and the total number of bins and positions of the left and right most histogram edges were then computed. Finally, the remaining bin edges were distributed uniformly between leftEdge and rightEdge at bandwidth intervals (Mathworks Website).

To compare sULM and micro-CT, we chose to represent the spatial distribution of glomeruli by the histogram of 20 bins for micro-CT and we fixed the constraint of the same bin width for both imaging methods. The statistical Kolmogorov-Smirnov test was done on these bins to compare the spatial distribution of sULM and micro-CT (Table 1).

On the micro-CT, the glomeruli perfused distribution width (PDW) was determined by calculating the full width at half maximum (FWHM) of the "global" glomerulus intensity profile (Supplementary Fig. 4). This intensity profile was calculated by summing all rows and columns from all glomeruli in a region of 20 pixels around its center, i.e., a 600-micrometers edge. Noisy glomeruli were removed from the calculation by selecting only those glomeruli that existed in four successive rotation of 90° of the same glomeruli. The intensity profile was then fitted by a Gaussian and interpolated, i.e. 600 points between -300 and 300 micrometers, before calculating the FWHM.

To estimate the glomeruli PDW on sULM, we took all slow tracks, i.e. tracked with slow sULM parameters, centered in zero belonging to the glomerular mask. We then took the FWHM of the "global" glomerulus density profile (Supplementary Fig. 4). This global density profile was calculated by summing all rows and columns from all glomeruli projected four times in the four directions - i.e. 90° rotation - in an interpolated grid of one µm for rats, and of 50µm for humans. The density profile was interpolated before calculating the FWHM, i.e. 600 points between -300 and 300µm for rats and 3000 points between -1500 and 1500µm for humans.

Statistical analysis

Statistical analyses were performed to evaluate the metrics between the different regions of the kidney using an unpaired two-sided parametric student's t-test with a 95% confidence level assuming a Gaussian distribution on GraphPad Prism 9 software. The significance of the scoring was explained by the following P values: ns = $P > 0{\cdot}05$, * = $P \leq 0{\cdot}05$, ** = $P \leq 0{\cdot}01$, *** = $P \leq 0{\cdot}001$, **** = $P \leq 0{\cdot}0001$.

Two-sided Kolmogorov-Smirnov nonparametric statistical tests[32] were also performed on the spatial distributions of glomeruli as a function of their distance from the renal capsule on sULM and micro-CT images with GraphPad Prism 9 software.

Role of funders

The funders had no role in the study design, data collection, data analysis, interpretation, or report writing. All of these steps were carried out by contributors described later. Olivier Couture is responsible for the decision to submit the manuscript.

Results

sULM highlighted spinning microbubbles in the rat kidney

Thanks to the double-filtering and the double-tracking explained above, we could obtain a composite sULM density map with slow tracks highlighted in pink and fast ones in green (Fig. 1d). The microvasculature reconstructed by sULM was much more resolved than with the Power Doppler of the same acquisition (Fig 1. c). In the sULM map, we could observe particular microbubble behavior in the cortex: microbubble tracks that entering and then exiting an area where they were spinning at velocities corresponding to the capillary flow. A zoom on the cortex in Fig. 1e confirmed the presence of these slow bundles of capillaries, i.e. the glomeruli. As an example, an independent microbubble was followed along this pathway leading to a glomerular shape in Fig. 1e and Fig. 1f. Other microbubbles within the cortex appeared to rise, then swirled before leaving again (Supplementary Videos 1-4, Supplementary Fig. 5). Such microbubble behavior has only been observed along the intermediate vessels of the cortex.

Segmentation of the different regions of the kidney, namely the medulla, main vessels, and cortex, are presented in Figure 1g. Glomerular mask constructed by including high normalized distance tracks is shown in Supplementary Fig. 5e. Metrics to highlight glomeruli, including normalized speeds - i.e. distance traveled by the track divided by the maximum speed in each area; remanence time - i.e. time duration of the track within a radius of 50µm from the track center; and dispersity - i.e. number of times that a track goes in the same direction divided by the number of points constituting the track; are displayed respectively in Fig. 1h, Fig. 1i and Fig. 1j. Tracks in the glomerular mask seemed specific to this area. They are slower, more stagnant, and less dispersed compared to tracks in the medullary region and in the main vessels. Statistical analyses showed that these differences were always significant from the main vessels to the glomeruli and from the main vessels to the medullary region, but these metrics were not significantly different between the medulla and the glomeruli (Table 2).

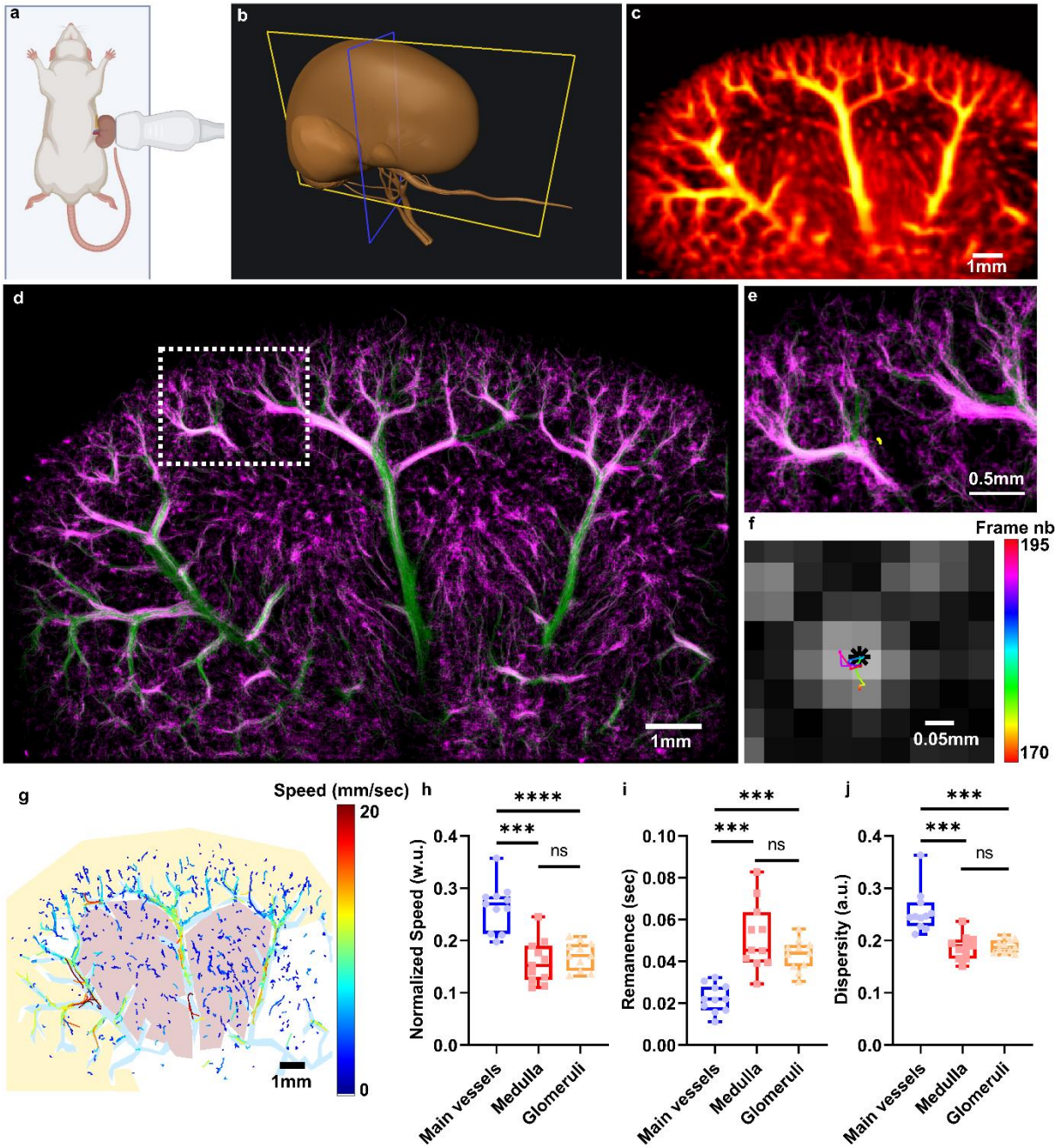

Figure 1. Glomerular structures were observed in the rat kidney cortex by sULM.

(a) Experimental setup. **(b)** The imaging plane is the yellow one. **(c)** Power Doppler of the rat 14. **(d)** sULM density map in rat 14 with superimposed slow-tracking (pink) and fast-tracking (green). **(e)** Zoom in the cortex area. **(f)** Zoom of yellow glomerular behavior highlighted in e. **(g)** Masks of the three regions in rat kidney: cortex (yellow), main vessels (blue), and medulla (red). 500 first slow and 500 first fast tracks encoded with speed are presented upon background masks. **(h)** Mean normalized speed of all tracks in 11 rats compared by region. The significance of the scoring is explained by the following P values: ns = $P > 0{\cdot}05$, * = $P \leq 0{\cdot}05$, ** = $P \leq 0{\cdot}01$, *** = $P \leq 0{\cdot}001$, **** = $P \leq 0{\cdot}0001$ (unpaired student's t-tests with a 95% confidence level). The center line corresponds to the median, box limits to upper and lower quartiles, whiskers to 1·5x interquartile range and no outliers have been considered. **(i)** Mean remanence time of all tracks in 11 rats compared by region. Same statistical tests. **(j)** Mean dispersity of all tracks in 11 rats compared by region. Same statistical tests.

Micro-CT confirms that these spinning microbubbles detected in sULM correspond to glomeruli

Figure 2a and Figure 2b show the sULM and the micro-CT of rat seven in the same longitudinal plane. Additional rats are shown in Supplementary Figure 2.

Figure 2c shows the glomeruli count using a high normalized distance value in the sULM and Figure 2d presents the glomeruli count using the selection of local high-intensity regional maxima on the micro-CT. Both imaging techniques appeared to show glomeruli in the same location.

In Figure 2e, we can see that the glomeruli spatial distributions from the kidney capsule were similar between the glomeruli detected by micro-CT, and the glomeruli observed by sULM in rat number seven (Figure 2f). Statistical analyses showed that these distributions came from the same continuous distribution in all rats (Supplementary Figure 6). Thus, the glomeruli were located at the same site.

Glomeruli's PDW for sULM and micro-CT appeared to be in the same order of magnitude (Fig 2. f) meaning that we observed the same phenomena with both modalities. Indeed, in all rats, PDW is 77±6 µm for sULM and 49±18µm for micro-CT (Table 3).

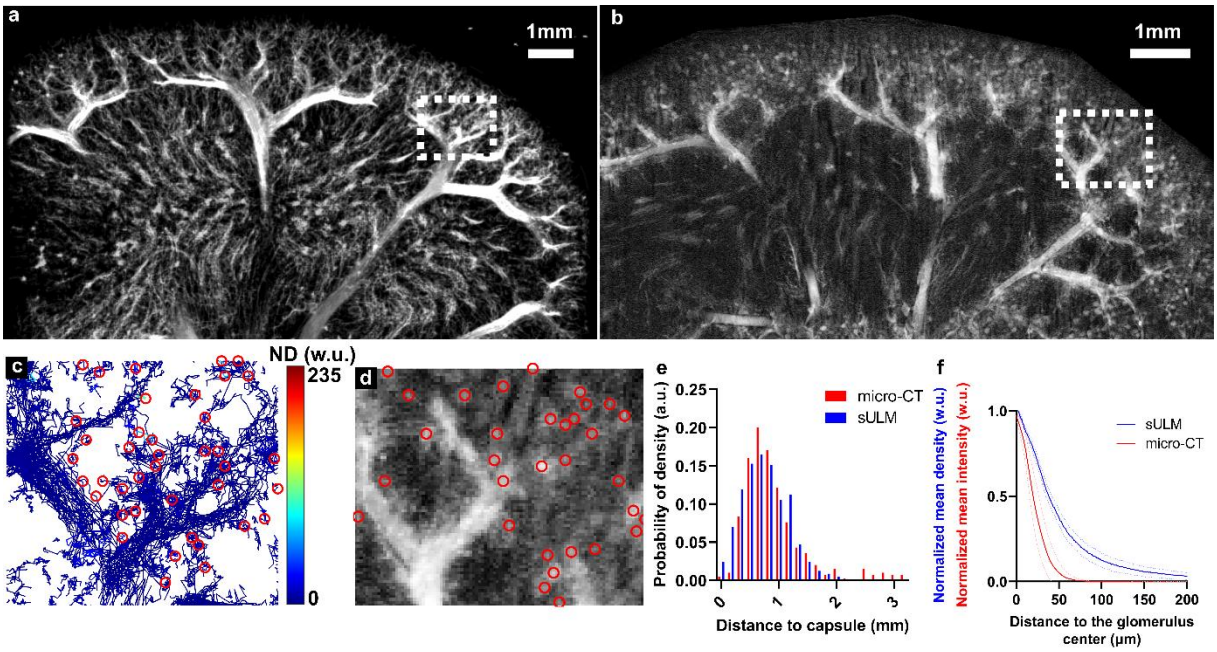

Figure 2. Capillary bundles observed in the sULM density map correspond to the glomeruli on micro-CT. **(a)** sULM density map in rat number seven. **(b)** Micro-CT in the same rat and same plane. **(c)** Zoom of sULM normalized distance (ND) map in rat seven (Methods). Red circles indicate glomerular count. 10,000 first slow and 5,000 first fast tracks encoded with ND are presented here. **(d)** Zoom of micro-CT in the same rat. Red circles indicate glomerular count. **(e)** Glomeruli count as a function of kidney capsule distance in micro-CT and sULM in rat seven (Methods). See Table 1 for more details on statistical analysis (two-sample Kolmogorov-Smirnov test). **(f)** Glomeruli PDW calculation with a density as a function of distance to the center of glomeruli (for sULM in blue, in 11 rats), and intensity as a function of the distance from the center pixel (micro-CT in red, in six rats). Dashed lines indicate standard deviation.

Glomeruli can also be observed in humans by sULM

Patient one's sULM composite density map presented the same glomerular shapes as rats in the cortex area (Fig. 3a). Another patient with the same cortical glomerular behavior is shown in Supplementary Figure 7.
A zoom in the cortex area confirmed the presence of arterioles with spinning microbubbles at the middle of their path, i.e. the glomeruli (Fig. 3b). Examples of glomeruli tracks are shown in yellow and red respectively in Figure 3c and 3d (Supplementary Videos 5-7).
The glomeruli count in sULM with the study of their PDW and of their spatial distribution from kidney capsules are presented in all patients in Supplementary Figure 8. We could observe that glomeruli PDW in humans were around 381±107µm (Table 4), which is bigger but in the same order of magnitude as the literature[20].
Manual segmentation of kidney areas is shown in Figure 3e, and the glomerular mask is presented in Supplementary Figure 7c. In the same way as in rats, glomeruli tracks remained slower (Fig. 3f), more stagnant (Fig. 3g), and less dispersed than the medullary region and the main vessels (Fig. 3h). The tracks inside the glomeruli therefore had a similar specific behavior in humans and in rats. Statistical analyses are detailed in Table 5.

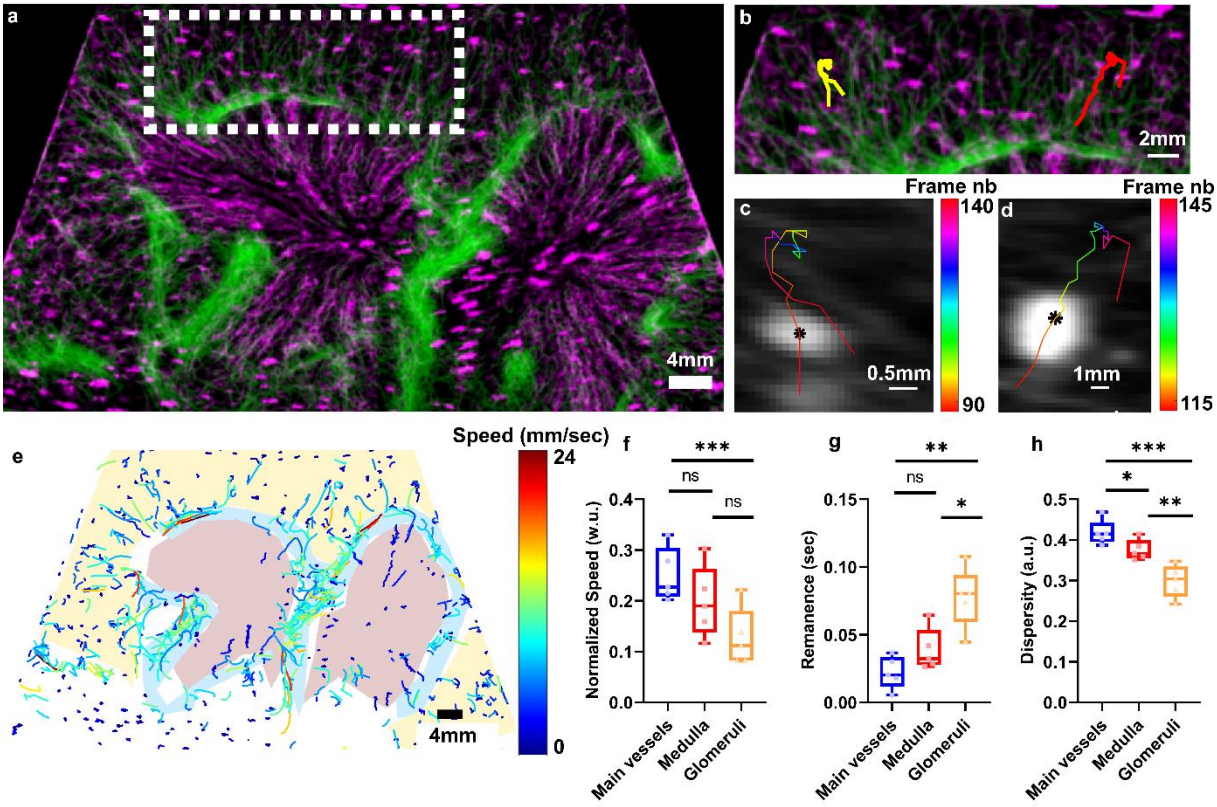

Figure 3. Glomeruli can be observed in the cortex of human kidneys by sULM.

(a) sULM density map in patient one with superimposed slow-tracking (pink) and fast-tracking (green). **(b)** Zoom in the cortex area. **(c)** Zoom of yellow track highlighted in b. **(d)** Zoom of red track highlighted in b. **(e)** Masks of the three regions: cortex (yellow), main vessels (blue), and medullary region (red). 500 first slow and 500 first fast tracks encoded with speed are presented upon background masks. **(f)** Mean normalized speed of all tracks in five patients compared by region. The significance of the scoring is explained by the following P values: ns = $P > 0{\cdot}05$, * = $P \leq 0{\cdot}05$, ** = $P \leq 0{\cdot}01$, *** = $P \leq 0{\cdot}001$, **** = $P \leq 0{\cdot}0001$ (unpaired student's t-tests with a 95% confidence level). The center line corresponds to the median, box limits to upper and lower quartiles, whiskers to 1·5x interquartile range and no outliers have been considered. **(g)** Mean remanence time of all tracks in five patients compared by region. Same statistical tests. **(h)** Mean dispersity of all tracks in five patients compared by region. Same statistical tests.

Discussion

In this study, we implemented a form of ULM which exploits the kinetic of individual microbubbles - including those flowing in the glomeruli - in order to map the renal microarchitecture of vessels. By classifying their behavior based on known anatomical features, we sought in this case the precise complexion of glomeruli microcirculation, including arterioles and capillaries. Spinning microbubbles were followed in the cortex and tracks analysis confirmed that these microbubbles are slower, more stagnant, and less dispersed than in the other kidney regions. The spatial distribution of glomeruli measured by sULM and by micro-CT belonged statistically to the same continuous distribution in six rats. Moreover, the glomeruli PDW measured by micro-CT and sULM was in the same order of magnitude with both techniques in all rats. Thanks to two these results and the fact that the micro-CT is considered to be the ex-vivo gold standard to observe microcirculation including inside glomeruli, we could conclude that glomeruli were observable by sULM.

These results allowed us to observe a part of individual glomeruli in living human grafts with a clinical imaging device, which was not possible with current imaging techniques[21–23]. We were not only able to observe a category of slow-moving microbubbles, but we showed how to reduce the gap between anatomical and functional imaging. This was done because we could image the very structures responsible for the function of the organ. By using sULM maps and the information given by the microbubble itself, we managed to image functional microvascular units. These kinds of observations will be essential to study many organs and diseases such as diabetes or cancer.

Still, this study has some limitations. The use of CEUS from a clinical ultrasound scanner has a frame rate between 14 and 64Hz, which implies bias in the estimation of the velocities for large vessels. The maximum velocity found in human sULM is 4cm/sec, whereas it is normally 100cm/sec[33,34]. Besides, glomeruli PDW measured by sULM are larger than the diameters found in the literature for humans[20,35,] and thinner for rats[30]. This is mainly because we did not measure the same information. With micro-CT and sULM, we measured the interval vascular system, i.e. the FWHM of the glomerular imaging task, whereas in the literature they measured the cellular content. Additional confirmation of the glomeruli distribution and size could later be obtained on immunostained histological sections.

For humans, the spatial resolution of CEUS, i.e. between 70 and 150µm, the localization error of 43±4µm - that increases with depth due to divergent ultrasound beam - and the presence of efferent and afferent arterioles in the same track as glomeruli leaded us to a rough PDW estimation with sULM (Supplementary Fig. 8, Supplementary Video 5 and 6). For rats, micro-CT perfusion was not always complete because of the complex injection procedure (Supplementary Table 2). Besides, fixation of the organ by PFA before scanning sometimes distorted the kidney, including vascular structures. Thus, the comparison between a living organ in sULM and a fixed organ in micro-CT is limited. Registrations of both techniques were done manually which also implies a bias. These points may explain the difference in PDW between sULM and micro-CT.

The observation of glomeruli in this study is only partial compared to results found in the literature[25,26,30,36–41] (Supplementary Table 4). On the one hand, this is due to a lack of acquisition time with the right concentration of microbubbles[42] (Supplementary Fig. 9). On the other hand, this is due to 2D sULM that limits the field of view to a unique imaging slice.

The 2D sULM also has the disadvantage of creating false out-of-plane tracks. These false tracks are mostly present in the medullary region because these regions were positioned transversely to the imaging plane used for

rats. Supplementary Fig. 10 shows these out-of-plane tracks inside the medulla in 4 rats. In humans, these out-of-plane tracks were less present because the clinician knew how to position the probe in the plane of the medullary vessels. These artefactual tracks could explain why the medulla tracks and the glomeruli tracks behave similarly in rats. Besides, medullary region is composed of capillaries within the vasa-recta and the juxtamedullary glomeruli, which can also explain the similarity between metrics in the medulla an in the glomeruli.

As another limitation, we can also mention the computational time which was multiplied by two due to the double tracking we performed to highlight the behavior of slow and fast microbubbles. These two regimes of microbubble behavior could not be followed in the same way, i.e. with the same tracking parameters. Indeed, if we had imposed the same tracking parameters for slow microbubbles as for fast microbubbles, i.e. high linking distances and short tracking time, then we would have risked matching microbubbles that did not belong to the same track or missing some microbubbles - because the parameters were not adapted to what we saw in the filtered acquisition that enhanced slow microbubbles. In the example of glomeruli, this could generate a deficit in their number.

In addition, movements were limited in this study because we had to externalize kidney in rats and because we had to include patients with shallower renal allografts (Supplementary Fig. 11). A future clinical trial to verify the feasibility of sULM on native human kidneys is hence needed.

In the future, 3D sULM[5,8,43,44] will also be needed to reduce and compensate for movements and to resolve the transverse direction, as encountered in the medullary region of rat acquisitions. Further studies will be necessary to analyze the behavior of microbubbles in more detail in the healthy and diseased glomeruli. Another study will be done to demonstrate the predictive diagnostic character based on glomerular sULM imaging. Furthermore, we believe that sULM might be a way to explore the vascular and functional status of various organs, not just kidneys. This approach could thus allow us to establish a diagnosis according to the individual behavior of each microbubble. This would eventually link macroscopic imaging and metabolism analyses.

Contributors

S.B., O.H., J.M.C., and V.H. contributed to the conception the human study. S.B. and V.H. contributed to the acquisition of the humans' sULM data. G.R., F.L., and O.C. contributed to the conception of the rats' study. A.A., L.D., S.B., F.L., G.R., and O.C. contributed to the acquisition of the rats' sULM data. A.A., L.D., S.B., F.L., G.R., and O.C. contributed to the acquisition of the micro-CT data. L.D., V.H., A.C. contributed to sULM and micro-CT post-processing. L.D., S.B., V.H., A.C., J.M.C., O.H., and O.C. contributed to the analysis and interpretation of the data. L.D., J.B., and O.C. contributed to the development of the Akebia software and the formatting of the codes. L.D., S.B., V.H., A.C., and O.C. contributed to drafting the manuscript. L.D., S.B., V.H., A.C., G.R., O.H., J.M.C, and O.C. contributed to revising the manuscript. L.D. and O.C. have direct access to the presented data. L.D. and O.C. have verified all the presented data.

All authors have read and approved the final version of the manuscript.

Declaration of Interest

O.C. and V.H., hold patents in the field of ultrasound localization microscopy (EP4011299A1). O.C. and V.H. are founders and shareholders of the ResolveStroke startup. O.C. has received several grants: ERC Consolidator grant agreement no 772786-Resolve Stroke, ERC POC (2022-2023), Maturation SATT Lutech for

ResolveStroke Startup, ANR FightClot, CNRS Prematuration for ResolveStroke Startup, RHU Quid NASH. O.C. gave a lecture at Bracco SAS and was an invited speaker at several conferences such as BMT Innsbruck. Other authors have no conflict of interest to disclose.

Acknowledgments

We thank the "Plateforme d'Imagerie du Vivant" (Université de Paris), and specifically Lotfi Slimani for the micro-CT acquisitions with the Skyscan 1172 Bruker.

This study was funded by the European Research Council under the European Union Horizon H2020 program (ERC Consolidator grant agreement No 772786-ResolveStroke).

Data Sharing Statement

ZENODO repository is accessible: https://zenodo.org/record/6811910#.ZA8Mkh-ZPic (DOI 10.5281/zenodo.6811910). All 60 blocks of rat 14 have been made available. To get the same image as in the article only blocks 10 to 20 and 27 to 32 have to be loaded (see README). This is due to the presence of motions on the last 28 blocks, and too many microbubbles at the beginning of the bolus (Methods). Patients' imaging data are not available due to ethical, medical, and legislative considerations toward personal information.

The GitHub repository is accessible with scripts and functions used to perform sULM. Matlab 2021a is needed to run the programs: https://github.com/EngineerJB/akebia. Moreover, a standalone application named Akebia, i.e. usable without a MATLAB license, is available in the same repository.

References

1. Errico C, Pierre J, Pezet S, Desailly Y, Lenkei Z, Couture O, et al., Ultrafast ultrasound localization microscopy for deep super-resolution vascular imaging. *Nature* **527**, 499–502 (2015).
2. Couture O, Hingot V, Heiles B, Muleki-Seya P, Tanter M., Ultrasound Localization Microscopy and Super-Resolution: A State of the Art. *IEEE Trans. Ultrason. Ferroelectr. Freq. Control* **65**, 1304–1320 (2018).
3. Christensen-Jeffries K, Couture O, Dayton PA, Eldar YC, Hynynen K, Kiessling F, et al., Super-resolution Ultrasound Imaging. *Ultrasound Med. Biol.* **46**, 865–891 (2020).
4. Tang S, Song P, Trzasko JD, Lowerison M, Huang C, Gong P, et al., Kalman Filter-Based Microbubble Tracking for Robust Super-Resolution Ultrasound Microvessel Imaging. *IEEE Trans. Ultrason. Ferroelectr. Freq. Control* **67**, 1738–1751 (2020).
5. Chavignon A, Heiles B, Hingot V, Orset C, Vivien D, Couture O, 3D Transcranial Ultrasound Localization Microscopy in the Rat Brain With a Multiplexed Matrix Probe. *IEEE Trans. Biomed. Eng.* **69**, 2132–2142 (2022).
6. Lowerison, M. R., Huang, C., Lucien, F., Chen, S. & Song, P., Ultrasound localization microscopy of renal tumor xenografts in the chicken embryo is correlated to hypoxia. *Sci. Rep.* **10**, 2478 (2020).
7. Taghavi I, Andersen SB, Søgaard SB, Nielsen MB, Sørensen CM, Stuart MB, et al., Automatic Classification of Arterial and Venous Flow in Super-resolution Ultrasound Images of Rat Kidneys. in 2021 *IEEE International Ultrasonics Symposium (IUS)* **1–3** (IEEE, 2021). doi:10.1109/IUS52206.2021.9593655.
8. Heiles B, Correia M, Hingot V, Pernot M, Provost J, Tanter M, et al., Ultrafast 3D Ultrasound Localization Microscopy Using a 32x32 Matrix Array. *IEEE Trans. Med. Imaging* **38**, 2005–2015 (2019).
9. Hingot, V., Errico, C., Tanter, M. & Couture, O. Subwavelength motion-correction for ultrafast ultrasound localization microscopy. *Ultrasonics* **77**, 17–21 (2017).
10. Tinevez, J.-Y. et al. TrackMate: An open and extensible platform for single-particle tracking. *Methods* **115**, 80–90 (2017).
11. Opacic T, Dencks S, Theek B, Piepenbrock M, Ackermann D, Rix A, et al., Motion model ultrasound localization microscopy for preclinical and clinical multiparametric tumor characterization. *Nat. Commun.* **9**, 1527 (2018).
12. Huang C, Lowerison MR, Trzasko JD, Manduca A, Bresler Y, Tang S, et al., Short Acquisition Time Super-Resolution Ultrasound Microvessel Imaging via Microbubble Separation. *Sci. Rep.* **10**, 6007 (2020).
13. Demené C, Robin J, Dizeux A, Heiles B, Pernot M, Tanter M, et al., Transcranial ultrafast ultrasound localization microscopy of brain vasculature in patients. *Nat. Biomed. Eng.* **5**, 219–228 (2021).
14. Desailly Y, Tissier AM, Correas JM, Wintzenrieth F, Tanter M, Couture O., Contrast enhanced ultrasound by real-time spatiotemporal filtering of ultrafast images. *Phys. Med. Biol.* **62**, 31–42 (2017).
15. Chmielewski. Renal anatomy and overview of nephron function. *Nephrol. Nurs. J.* **30**, 185 (2003).
16. Kanzaki, G., Tsuboi, N., Shimizu, A. & Yokoo, T. Human nephron number, hypertension, and renal pathology. *Anat. Rec. Hoboken NJ 2007* **303**, 2537–2543 (2020).
17. Tonneijck L, Muskiet MHA, Smits MM, van Bommel EJ, Heerspink HJL, van Raalte DH, et al., Glomerular Hyperfiltration in Diabetes: Mechanisms, Clinical Significance, and Treatment. *J. Am. Soc. Nephrol. JASN* **28**, 1023–1039 (2017).

18. Segelmark, M. & Hellmark, T. Autoimmune kidney diseases. *Autoimmun. Rev*. **9,** A366-371 (2010).
19. Kim Y, Lee S, Lee Y, Kang MW, Park S, Park S, et al., Glomerular Hyperfiltration and Cancer: A Nationwide Population-Based Study. Cancer Epidemiol. Biomark. *Prev. Publ. Am. Assoc. Cancer Res. Cosponsored Am. Soc. Prev. Oncol.* **29**, 2070–2077 (2020).
20. Samuel, T., Hoy, W. E., Douglas-Denton, R., Hughson, M. D. & Bertram, J. F. Applicability of the glomerular size distribution coefficient in assessing human glomerular volume: the Weibel and Gomez method revisited. *J. Anat.* **210**, 578–582 (2007).
21. Kassirer. Clinical Evaluation of Kidney Function - Glomerular Function. *N. Engl. J. Med.* **285**, 385–389 (1971).
22. Rahn, K. H., Heidenreich, S. & Brückner, D. How to assess glomerular function and damage in humans: *J. Hypertens.* **17**, 309–317 (1999).
23. Inker LA, Eneanya ND, Coresh J, Tighiouart H, Wang D, Sang Y, et al., New Creatinine- and Cystatin C–Based Equations to Estimate GFR without Race. *N. Engl. J. Med.* **385**, 1737–1749 (2021).
24. Andersen SB, Taghavi I, Kjer HM, Søgaard SB, Gundlach C, Dahl VA, et al., Evaluation of 2D super-resolution ultrasound imaging of the rat renal vasculature using ex vivo micro-computed tomography. *Sci. Rep.* **11**, 24335 (2021).
25. Xie L, Koukos G, Barck K, Foreman O, Lee WP, Brendza R, et al., Micro-CT imaging and structural analysis of glomeruli in a model of Adriamycin-induced nephropathy. *Am. J. Physiol.-Ren. Physiol.* **316**, F76–F89 (2019).
26. Hlushchuk R, Zubler C, Barré S, Correa Shokiche C, Schaad L, Röthlisberger R, et al., Cutting-edge microangio-CT: new dimensions in vascular imaging and kidney morphometry. *Am. J. Physiol.-Ren. Physiol*. **314**, F493–F499 (2018).
27. Blery P, Pilet P, Vanden-Bossche A, Thery A, Guicheux J, Amouriq Y, et al., Vascular imaging with contrast agent in hard and soft tissues using microcomputed-tomography. *J. Microsc.* **262**, 40–49 (2016).
28. Heiles B, Chavignon, Arthur, Hingot V, Lopez, Pauline, Teston, Eliott, Couture O. Open Platform for Ultrasound Localization Microscopy: performance assessment of localization algorithms. *Nat. Biomed. Eng.* **6**, 605–616 (2022).
29. Kuhn, H. W. The Hungarian method for the assignment problem. *Nav. Res. Logist. Q.* **2**, 83–97 (1955).
30. Baldelomar, E. J., Charlton, J. R., Beeman, S. C. & Bennett, K. M. Measuring rat kidney glomerular number and size in vivo with MRI. *Am. J. Physiol.-Ren. Physiol*. **314**, F399–F406 (2018).
31. Shelton SE, Lee YZ, Lee M, Cherin E, Foster FS, Aylward SR, et al., Quantification of microvascular tortuosity during tumor evolution using acoustic angiography. *Ultrasound Med. Biol.* **41**, 1896–1904 (2015).
32. Lehmann, E. L. & D'Abrera, H. J. Nonparametrics: statistical methods based on ranks. (*Holden-day*, San Francisco, United State,1975).
33. Pellerito, J. & Polak, J. Introduction to vascular ultrasonography. (*Elsevier Health Sciences*, Amsterdam, Europe, 2019).
34. Al-Katib, S., Shetty, M., Jafri, S. M. A. & Jafri, S. Z. H. Radiologic Assessment of Native Renal Vasculature: A Multimodality Review. *RadioGraphics* **37**, 136–156 (2017).

549 35. Puelles VG, Zimanyi MA, Samuel T, Hughson MD, Douglas-Denton RN, Bertram JF, et al., Estimating
550 individual glomerular volume in the human kidney: clinical perspectives. *Nephrol. Dial. Transplant.* **27**, 1880–
551 1888 (2012).
552 36. Bonvalet JP, Champion M, Courtalon A, Farman N, Vandewalle A, Wanstok F., Number of glomeruli
553 in normal and hypertrophied kidneys of mice and guinea-pigs. *J. Physiol.* **269**, 627–641 (1977).
554 37. Cullen-McEwen, L. A., Kett, M. M., Dowling, J., Anderson, W. P. & Bertram, J. F. Nephron Number,
555 Renal Function, and Arterial Pressure in Aged GDNF Heterozygous Mice. *Hypertension* **41**, 335–340 (2003).
556 38. Geraci S, Chacon-Caldera J, Cullen-McEwen L, Schad LR, Sticht C, Puelles VG, et al., Combining new
557 tools to assess renal function and morphology: a holistic approach to study the effects of aging and a congenital
558 nephron deficit. *Am. J. Physiol.-Ren. Physiol.* **313**, F576–F584 (2017).
559 39. Klingberg A, Hasenberg A, Ludwig-Portugall I, Medyukhina A, Männ L, Brenzel A, et al., Fully
560 Automated Evaluation of Total Glomerular Number and Capillary Tuft Size in Nephritic Kidneys Using
561 Lightsheet Microscopy. *J. Am. Soc. Nephrol*. **28**, 452–459 (2017).
562 40. Murawski, I. J., Maina, R. W. & Gupta, I. R. The relationship between nephron number, kidney size
563 and body weight in two inbred mouse strains. *Organogenesis* **6**, 189–194 (2010).
564 41. Perrien DS, Saleh MA, Takahashi K, Madhur MS, Harrison DG, Harris RC, et al, Novel methods for
565 microCT-based analyses of vasculature in the renal cortex reveal a loss of perfusable arterioles and glomeruli in
566 eNOS-/- mice. *BMC Nephrol*. **17**, 24 (2016).
567 42. Hingot V, Errico C, Heiles B, Rahal L, Tanter M, Couture O., Microvascular flow dictates the
568 compromise between spatial resolution and acquisition time in Ultrasound Localization Microscopy. *Sci. Rep*. **9**,
569 2456 (2019).
570 43. Jensen JA, Ommen ML, Oygard SH, Schou M, Sams T, Stuart MB, et al., Three-Dimensional Super-
571 Resolution Imaging Using a Row–Column Array. IEEE Trans. Ultrason. Ferroelectr. Freq. Control 67, 538–546
572 (2020).
573 44. Harput S, Christensen-Jeffries K, Ramalli A, Brown J, Zhu J, Zhang G, et al., 3-D Super-Resolution
574 Ultrasound Imaging With a 2-D Sparse Array. *IEEE Trans. Ultrason. Ferroelectr. Freq. Control* **67**, 269–277
575 (2020).
576

577 **Tables**

578

579 **Table 1. A detailed comparison between glomeruli spatial distribution in micro-CT and in sULM[32]**

Test statistic	Metric	Rat number	Confidence Intervals micro-CT	Confidence Intervals sULM	Size (n)	Kolmogorov-Smirnov D	P-value
Two-sample Kolmogorov-Smirnov test	Glomeruli spatial distribution between micro-CT and sULM	7	0·02 To 0·08	0·02 To 0·08	20	0·30	0·33
		8	0·03 To 0·07	0·03 To 0·07	20	0·20	0·82
		11	0·03 To 0·07	0·03 To 0·07	20	0·20	0·82
		12	0·03 To 0·07	0·02 To 0·08	20	0·40	0·08
		13	0·03 To 0·08	0·02 To 0·08	20	0·35	0·17
		15	0·03 To 0·07	0·03 To 0·06	20	0·25	0·56

580

581 **Table 2. A detailed comparison between main vessels, medulla, and glomeruli in rats**

Test statistic	Metric	Region compared	Confidence intervals	Size (n)	Degrees of freedom	P-value
Two-sided student t-test	Normalized Speed	Main vessels and medulla	-0·14 to -0·07	11	10	<0·001
		Main vessels and glomeruli	-0·13 to -0·06	11	10	<0·0001
		Medulla and glomeruli	-0·02 to 0·04	11	10	0·39
	Remanence	Main vessels and medulla	0·02 to 0·04	11	10	<0·001
		Main vessels and glomeruli	0·02 to 0·03	11	10	<0·001
		Medulla and glomeruli	-0·02 to 0·00	11	10	0·12
	Dispersity	Main vessels and medulla	-0·09 to -0·04	11	10	<0·001
		Main vessels and glomeruli	-0·09 to -0·04	11	10	<0·001
		Medulla and glomeruli	-0·01 to 0·02	11	10	0·80

582

583 **Table 3. Glomeruli PDW estimation by sULM and by micro-CT in rats**

Rat n°	sULM (µm)	Micro-CT (µm)
1	80	/
2	74	/
5	65	/
6	74	/
7	76	67
8	75	56
11	75	49
12	88	36
13	85	46
14	78	/
15	83	43
Mean ± std	78 ± 6	49 ± 18

584

585 **Table 4. Glomeruli PDW estimation by sULM in patients**

Patient n°	sULM (µm)
1	389
2	236
3	203
4	462
13	372
Mean ± std	332 ± 109

586

587 **Table 5. A detailed comparison between main vessels, medulla, and glomeruli in humans**

Test statistic	Metric	Region compared	Confidence intervals	Size (n)	Degrees of freedom	P-value
Two-sided student t-test	Normalized Speed	Main vessels and medulla	-0·14 to 0·04	5	4	0·22
		Main vessels and glomeruli	-0·20 to 0·04	5	4	0·01
		Medulla and glomeruli	-0·16 to 0·02	5	4	0·12
	Remanence	Main vessels and medulla	0·00 to 0·04	5	4	0·09
		Main vessels and glomeruli	0·03 to 0·08	5	4	0·00
		Medulla and glomeruli	0·01 to 0·07	5	4	0·01
	Dispersity	Main vessels and medulla	-0·08 to 0·00	5	4	0·04
		Main vessels and glomeruli	-0·17 to 0·07	5	4	<0·001
		Medulla and glomeruli	-0·13 to 0·03	5	4	0·01

588

Figure Legends

Figure 1. Glomerular structures were observed in the rat kidney cortex by sULM.
(a) Experimental setup. **(b)** The imaging plane is the yellow one. **(c)** Power Doppler of the rat 14. **(d)** sULM density map in rat 14 with superimposed slow-tracking (pink) and fast-tracking (green). **(e)** Zoom in the cortex area. **(f)** Zoom of yellow glomerular behavior highlighted in e. **(g)** Masks of the three regions in rat kidney: cortex (yellow), main vessels (blue), and medulla (red). 500 first slow and 500 first fast tracks encoded with speed are presented upon background masks. **(h)** Mean normalized speed of all tracks in 11 rats compared by region. The significance of the scoring is explained by the following P values: ns = $P > 0{\cdot}05$, * = $P \leq 0{\cdot}05$, ** = $P \leq 0{\cdot}01$, *** = $P \leq 0{\cdot}001$, **** = $P \leq 0{\cdot}0001$ (unpaired student's t-tests with a 95% confidence level). The center line corresponds to the median, box limits to upper and lower quartiles, whiskers to 1·5x interquartile range and no outliers have been considered. **(i)** Mean remanence time of all tracks in 11 rats compared by region. Same statistical tests. **(j)** Mean dispersity of all tracks in 11 rats compared by region. Same statistical tests.

Figure 2. Capillary bundles observed in the sULM density map correspond to the glomeruli on micro-CT.
(a) sULM density map in rat number seven. **(b)** Micro-CT in the same rat and same plane. **(c)** Zoom of sULM normalized distance (ND) map in rat seven (Methods). Red circles indicate glomerular count. 10,000 first slow and 5,000 first fast tracks encoded with ND are presented here. **(d)** Zoom of micro-CT in the same rat. Red circles indicate glomerular count. **(e)** Glomeruli count as a function of kidney capsule distance in micro-CT and sULM in rat seven (Methods). See Table 1 for more details on statistical analysis (two-sample Kolmogorov-Smirnov test). **(f)** Glomeruli PDW calculation with a density as a function of distance to the center of glomeruli (for sULM in blue, in 11 rats), and intensity as a function of the distance from the center pixel (micro-CT in red, in six rats). Dashed lines indicate standard deviation.

Figure 3. Glomeruli can be observed in the cortex of human kidneys by sULM.
(a) sULM density map in patient one with superimposed slow-tracking (pink) and fast-tracking (green). **(b)** Zoom in the cortex area. **(c)** Zoom of yellow track highlighted in b. **(d)** Zoom of red track highlighted in b. **(e)** Masks of the three regions: cortex (yellow), main vessels (blue), and medullary region (red). 500 first slow and 500 first fast tracks encoded with speed are presented upon background masks. **(f)** Mean normalized speed of all tracks in five patients compared by region. The significance of the scoring is explained by the following P values: ns = $P > 0{\cdot}05$, * = $P \leq 0{\cdot}05$, ** = $P \leq 0{\cdot}01$, *** = $P \leq 0{\cdot}001$, **** = $P \leq 0{\cdot}0001$ (unpaired student's t-tests with a 95% confidence level). The center line corresponds to the median, box limits to upper and lower quartiles, whiskers to 1·5x interquartile range and no outliers have been considered. **(g)** Mean remanence time of all tracks in five patients compared by region. Same statistical tests. **(h)** Mean dispersity of all tracks in five patients compared by region. Same statistical tests.

Supplementary Materials

This paper contains supplementary material available online.

Correspondence and requests for materials should be addressed to:

Louise Denis: louise.denis@sorbonne-universite.fr

Olivier Couture: olivier.couture@sorbonne-universite.fr